Ceramics International 42 (2016) 15023–15029

Contents lists available at ScienceDirect

Ceramics International

journal homepage: www.elsevier.com/locate/ceramint

Electrical behavior of cerium dioxide films exposed to different gases atmospheres

R.C. Deus [a], R.A.C. Amoresi [b,*], P.M. Desimone [c], F. Schipani [c], L.S.R. Rocha [a], M.A. Ponce [c], A.Z. Simoes [a], E. Longo [b]

[a] Faculty of Engineering of Guaratinguetá, São Paulo State University – UNESP, Av. Dr Ariberto Pereira da Cunha 333, Bairro Pedregulho, P.O. Box 355, 12.516-410 Guaratinguetá, SP, Brazil

[b] Interdisciplinary Laboratory of Electrochemistry and Ceramics, LIEC – Chemistry Institute, São Paulo State University – UNESP, Prof. Francisco Degni Street, 55, Quitandinha, 14800-060 Araraquara, SP, Brazil

[c] Research Institute of Materials Science and Technology (INTEMA), National University of Mar del Plata (CONICET), Juan B. Justo Street 4302, 7600 Mar del Plata, Argentina

ARTICLE INFO

Article history:
Received 22 February 2016
Received in revised form
29 April 2016
Accepted 23 June 2016
Available online 23 June 2016

Keywords:
A. Films
B. Defects
C. Chemical properties
D. CeO_2
E. Sensors

ABSTRACT

Here we present an easy-reproducible microwave-assisted hydrothermal route for preparing pure nanocrystalline CeO_2 films. The produced materials were characterized using a wide range of techniques (X-ray diffraction, field emission gun scanning electron microscopy, Raman spectroscopy) to understand the synthesis dependent changes in crystallographic structure, and crystallite size. Raman and X-ray diffraction techniques revealed that the films were free of secondary phases and that they crystallize in the cubic structure. The observed hydrodynamic particle size larger than the crystallite size confirms the aggregation phenomenon. Gas sensing measurements have been carried out to rationalize the type and number of surface adsorbed groups and overall nanostructure. Electrical conductance variations, owing to gases adsorption onto semiconductor oxide films surfaces, were observed in this work. Chemiresistive CeO_2 film properties depend on the intergranular barrier heights and width.

© 2016 Elsevier Ltd and Techna Group S.r.l. All rights reserved.

1. Introduction

Controlling the crystal structure of materials films at nanoscale is critical for developing high-performance functionalities [1–4]. In particular, cerium dioxide (CeO_2, ceria) [5] is a technologically important ceramic material, widely for multiple purposes among them including catalysts, solid electrolytes, and gas sensors [6,7]. Different preparation methods have been reported to obtain CeO_2 nanopowders, such as thermal evaporation technique [8], sol-gel method [9], and the hydrothermal route [10] which proved its efficacy for the synthesis of 3D hierarchical architectures [11]. Although various types of nanostructures have been synthesized, it still remains a challenge to perform shape-controlled synthesis with well defined morphology and uniform size. Also, it is well known that owing in a reduction in the grain size of the nanostructured sensing materials, surface-to-volume ratio increases, therefore, creating more active surfaces. In spite of technological progress, and the fact that the grain size determines the main operating characteristics of sensors such as the magnitude and the rate of response [12], basic understanding of semiconductor gas sensors have also depened through the elucidation of the role of Schottky barriers and adsorbed oxygen, grain size effects, chemical, and electronic sensitization mechanisms [13]. Maekawa et al. [14] have determined that the sensitivity and selectivity to gases depends largely on the grain size, showing that the selectivity is improved by its grown.

Gas sensors are foreseen as a porous sensing layer of a semiconductor oxide, which oxygen diffuses, being adsorbed on the grain surface. It is known that the n-type semiconducting behavior of CeO_2 is due to oxygen vacancies that act as donors. In these materials, the electrical conduction is determined by the grain boundary barrier parameters (height and width) which depend on the amount of chemisorbed species. Particularly, chemisorbed oxygen from the atmosphere forms charged species, trapping electrons at the grain boundaries, and consequently modifying the potential barriers. Reducing gases remove some of the adsorbed oxygens, altering the potential barriers, and consequently the overall conductivity, originating a measurable electrical signal [15–17].

Furthermore, in contrast to classic solid state syntheses methods, microwave-assisted hydrothermal (MAH) method require

* Corresponding author.
E-mail address: rafaelciola@yahoo.com.br (R.A.C. Amoresi).

http://dx.doi.org/10.1016/j.ceramint.2016.06.151
0272-8842/© 2016 Elsevier Ltd and Techna Group S.r.l. All rights reserved.

comparably lower temperatures and therefore less energy, while at the same time producing high quality nanocrystalline samples. The irradiation of microwaves inside the solution causes rapid internal heating by the direct coupling of microwave energy with the molecules, which also helps to form flake morphology with reduced agglomeration. This method has been utilized by our group to synthetize CeO_2 [19]. In this context, nanoparticles synthesized by MAH method under NH_4OH revealed agglomerate particles, while the ones synthesized under MAH conditions with KOH or NaOH mineralizer agents were well-dispersed and homogeneously distributed. This can be explained by the amount of hydrogen bonds, formed during the MAH process, making it harder for the particles to agglomerate. Ultraviolet-visible (UV–vis) spectra revealed the presence of localized energy levels into the band gap of CeO_2 powders with a soaking time of 4 and 8 min, possibly due to certain structural disorder degree in the lattice [15,16,18]. The sample obtained at 8 min showed the best crystallization. Remarkable efforts regarding the preparation of CeO_2 nanoparticles with the MAH route was devoted by our group, and afterwards its photoluminescent emission as a function of La content was analyzed. The polycrystalline samples presented two peaks: at 490 nm (blue-green emission) and the other at 610 nm (green emission); a behavior that is likely associated with the structure organization level and the charge transfer occurring between oxygen and cerium ions, displaying that its addition causes changes in the defects or disorder of materials, consequently affecting the particle sizes [18–20].

In this work, the focus is the controllable synthesis of undoped CeO_2 sphere-like nanostructures through the straightforward MAH process in order to conform and analyze the electrical behavior of thick films in air and CO atmospheres, under different temperatures. Samples were characterized by X-Ray diffraction (XRD), Raman Spectroscopy and Field emission gun scanning electron microscopy (FEG-SEM) techniques. Finally, a theoretical explanation is given to correlate the concentration of defects in the films and its barrier height (eV), in parallel with the tunneling and thermionic current contributions.

2. Experimental procedure

Pure CeO_2 powders were synthesized by the MAH route. Ammonium cerium (IV) nitrate (5×10^{-3} mol L^{-1} $Ce(NH_4)_2(NO_3)_6$, 99.9% purity) was dissolved in 80 mL of deionized water under constant stirring for 15 min at 70 °C. The solution had its pH adjusted to 10, under constant stirring at room temperature, through the addition of KOH (2 mol L^{-1}, 99.5% purity – Synth). The resulted solution was transferred into a sealed Teflon autoclave and placed in a microwave hydrothermal oven (2.45 GHz, maximum power of 800 W). The reactional system was heat treated at 100 °C with a soaking time of 1, 2, 4, and 8 min with a heating rate fixed at 10 °C/min. The maximum pressure reached in the sealed autoclave was ~1.2 atm. The autoclave was cooled to room temperature naturally. CeO_2 powders (labeled as P_i, for i = 1, 2, 4, and 8 min) were centrifuged and washed with deionized water, and then dried at 100 °C in an oven for 48 h. The obtained powders were used to make cerium oxide films (F_i for i = 1, 2, 4, and 8 min). The powders particle size distributions were determined by the hydrodynamic particle size technique using liquid media. Then, a paste was prepared with an organic binder (glycerol) using P_8 powders. The used solid/organic binder ratio was 1.2/1. No dopants were added. Thick porous films were made by screen-printing technique onto 96% dense insulating alumina substrates, on which electrodes with an interdigitated shape had been delineated by sputtering. An adhesion layer consisting of 25 nm titanium was deposited and, without breaking vacuum, a platinum 200 nm film was deposited over the Ti layer. For defining the interdigitated electrodes, the substrates with the metal films were placed in a home-built micromachining laser. Later, films were thermally treated in dry air atmosphere up to 380 °C and maintained at this temperature for 2 h, using a heating rate of 1 °C/min in order to evaporate the binder. The films thickness of the was measured with a Surtronic 3+(Taylor Hobson) profilometer with a diamond stylus (radius: 1 μm) and the cross section was analyzed using SEM microscopy. Films were characterized using X-Ray diffraction (XRD), with a PANalytical X'Pert PRO diffraction system employing CuKα radiation (λ=0.1542 nm) at 40 kV as generator tension and 40 mA as generator current. The samples were scanned in the 2θ range of 20–90° at 0.02°/min. The XRD data were analyzed using X'Pert PRO HighScore software. To image the cerium oxide surfaces, a JEOL JSM 6460-S scanning electron microscope was employed.

Raman spectra were acquired at room temperature with a Renishaw in Via Reflex micro-spectrometer equipped with a charge-coupled device detector (CCD; 1024 × 256 pixels). An Ar laser line (514 nm, 50 mW) was used as the excitation source in combination with a grating of 2400 grooves/mm. A 50X (0.50 NA) Leica metallurgical objective was used in the excitation and collection paths. A neutral density filter was used to reduce the incident laser power on the sample to values of about 0.2 mW, as measured with a silicon photodiode (Coherent Inc.). In those conditions, the sampled volume has a lateral dimension below 1.5–2 μm. The sampled depth was less than 1.5 μm, as determined by z-scanning a silicon wafer above and below its surface.

The electrical characterization of films (overlapped or non overlapped potential barriers) was monitored using an HP4284A impedance analyzer. The measurements were carried out at a frequency interval from 20 Hz to 1 MHz. Later, the electrical resistances of the films were measured during modifications in the temperature in the range of 25–230 °C at a rate of ~ 2 °C/min in vacuum, dry air (760 mmHg), and 100 mmHg CO atmosphere. Also, in order to obtain the most favorable temperature in which the sensors presents the best time response and sensitivity when the atmosphere change from vacuum to air and from vacuum to CO, measurements of resistance vs. time were carried out. Measurements were done when samples get to steady state and no changes in resistance over time were observed. An Agilent 3440A multimeter was used for the electrical conductance measurements.

3. Results and discussion

Fig. 1a illustrates the X-Ray diffraction patterns of pure CeO_2 syntheiszed under MAH at 100 °C for different times (t=1, 2, 4 and 8 min) prepared with KOH. XRD results confirmed that powders with different times of synthesis exhibit similar behavior. Analyzing the diffraction patterns of the crystalline samples shown in Fig. 1, it is found that powders showed the same crystalline structure for all the synthesis conditions used. All peaks can be well-indexed in a pure cubic structure of CeO_2 (space group: Fm3m) with lattice constant a=5.411 Å, which is in good agreement with the JCPDS file for CeO_2 (JCPDS 34-394). Overall, the diffraction peaks of P_8 are more intense than the others synthesized powders, indicating that the P_8 powder has a better crystal quality that the others. The average crystallite sizes calculated by Debye Scherrer were 6.3, 9.1, 12.8 and 13.6 nm for P_1, P_2, P_4 and P_8, respectively. Fig. 1b illustrates that the hydrodynamic particle size of P_8 is larger than the crystallite size and confirms the aggregation phenomenon. The powders are composed of double-dispersed particles with a hydrodynamic average diameter particle size of approximately 32 nm (P_8). The theoretical number of crystallites by particle, determined by the hydrodynamic particle

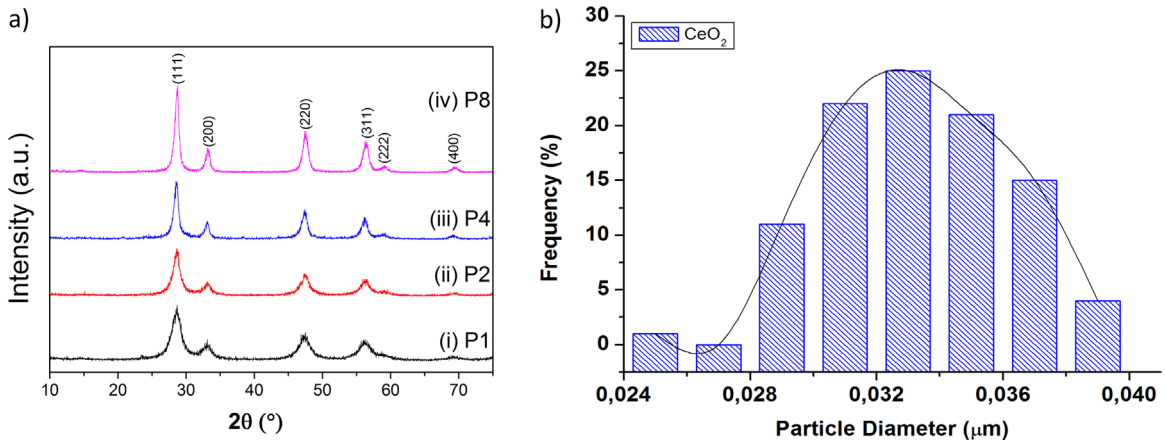

Fig. 1. (a) X-ray diffraction patterns of powders synthesized from the nanoparticles obtained at 100 °C in the MAH method under KOH mineralizer at different soaking times: (i) P_1, (ii) P_2, (iii) P_4 and (iv) P_8. (b) hydrodynamic particle size distribution of P_8.

size, to crystallite size ratio is nearly constant. This may be explained by the fact that the powders were calcined at the same temperature and during same time and may indicate a constant sintering process.

The formation of pure CeO_2 at different times of synthesis was also confirmed by Raman spectroscopy (Fig. 2). Cubic fluorite structure-metal dioxides have a single Raman mode at 461 cm^{-1}, which has F_{2g} symmetry and can be viewed as a first-order symmetric stretching mode of the Ce-O_8 vibrational unit. A comparison of the spectra at different times of synthesis showed that the bandwidth of this peak decreases with soaking time which can be inferred that there is an increase on particle size and therefore an increase of the order of the interior lattice structure as the soaking time increases [21]. The Raman spectrum of nanocrystallite CeO_2 at different soaking times also have shown a small peak at 253 cm^{-1} which can be attributed to size effects [22]. From Fig. 2 it can be seen that the relative intensity of this peak decreases with an increase in crystallite size. Therefore, peak at 461 cm^{-1} can be attributed to the interior phonon modes of the crystal, whereas peak at 253 cm^{-1} is a phonon mode related to the surface layer of the crystal. Weaker Raman bands are also observed at 603 and 1170 cm^{-1} due to defect-induced mode and second-order longitudinal optical (2LO) mode, respectively [23,24]. The relative intensity ratio of I_{603}/I_{461} follows the sequence P_1; P_2; P_4; P_8, indicating that the P_1 powder has the most intrinsic defect sites while P_8 powder has the least.

The Raman bands at 740 and 1050 cm^{-1} on CeO_2 powders are due to residue nitrate species left from the synthesis process [23].

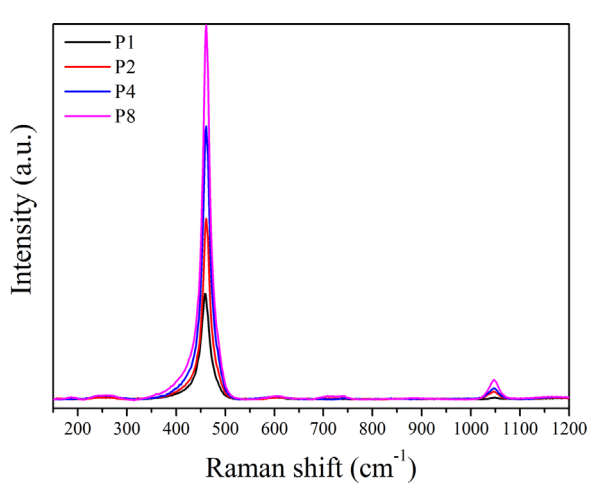

Fig. 2. Raman spectrum of powders synthesized at different soaking times.

An analysis of the result displayed in Fig. 2 shows that all peak positions of different soaking times remain invariant and an increase in intensity of all Raman peaks is observed as the soaking time is increased. These results indicates that the time of synthesis influences the powder crystallinity. Overall, the Raman peaks of P_8 are more intense than the others powders, indicating that the P_8 powder has a better crystal quality than P_1, P_2 and P_4. At this point, the results by Raman spectroscopy are totally consistent with those obtained by XRD.

Fig. 3a and b show the SEM images of the CeO_2 thick films. According to the image (a), most of the grains of CeO_2 films are homogeneous with an average agglomerate size of 430 nm. The undoped CeO_2 powders display poor contrast and intense agglomeration among extremely fine particles. The higher agglomeration degree of undoped CeO_2 is due the Van der Waal's force derived for the –OH ligand precursor which was transformed to CeO_2 after hydrothermal treatment. Moreover, the distribution in size seemed to be homogeneous and with rounded-shape appearance The as-synthesized CeO_2 grains sizes were relatively spherical with uniform size distribution. Fig. 3b shows the film cross section with a film average thickness of 110 μm.

Sensitivity was measured for different temperatures as a function of R_{gas}/R_v, where R_{gas} corresponds to the resistance of films when they reach an equilibrium state after oxygen or CO exposition, at different temperatures as a function of time, and R_v, the resistance of films in vacuum. Different resistances vs. time curves for different temperatures were carried out. In Fig. 4 the sensitivity vs. temperature curves for F_8 is presented. An analysis of the results renders that the films display an increase of the sensitivity (for air exposure R_{gas}/R_v) as temperature rise above 250 °C. This behavior could be associated with the oxygen adsorption in the particles surfaces which produces a decrease in the sample conductivity. In this case, oxygen adsorption produces an increasing in the potential barrier height and then a reduction in the sample conductivity is observed. Also, at temperatures below 280 °C, oxygen diffusion into the grains is not significant. At temperatures greater than 300 °C, an increase of the sensitivity could be also associated with the oxygen diffusion into the grain and oxygen vacancies annhilation in the bulk. When the atmosphere is changed from vacuum to CO, a mild increase of the electrical resistance is observed for F_8 sample. Despite the amount of CO incorporated to the chamber, there is not a great reaction (electrical resistance decreasing) if samples are previously treated with vacuum as a consequence of oxygen desorption from the surface. It is well known that the temperature where CO reaction with oxygen takes place is over 250 °C. From Fig. 4, in the whole temperatures range, the sensitivity for CO exposure is greater than

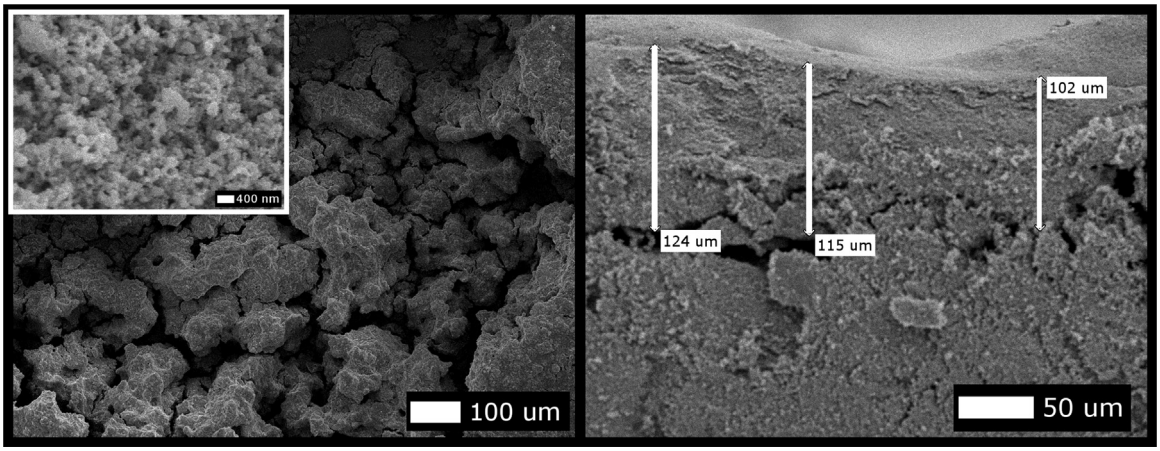

Fig. 3. Field emission gun scanning electron microscopy of films (F_8) obtained from the nanoparticles synthesized at 100 °C in the MAH method under KOH mineralizer. Surface (a) and cross-section view (b).

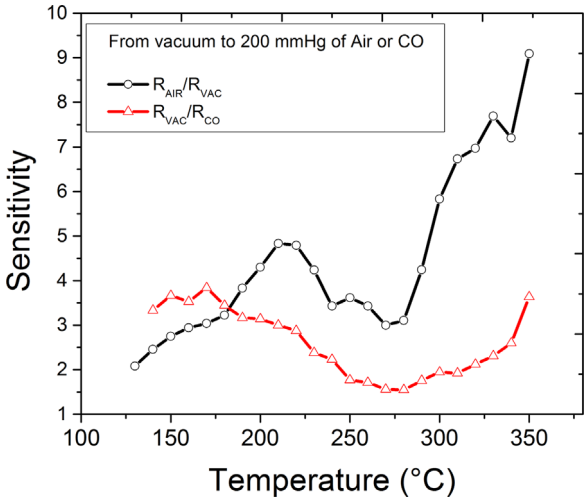

Fig. 4. Film (F_8) sensitivity (R_{air}/R_{vacuum} and R_{vacuum}/R_{CO}) versus temperature for films synthesized from the nanoparticles obtained at 100 °C, t=8 min in the MAH method under KOH mineralizer.

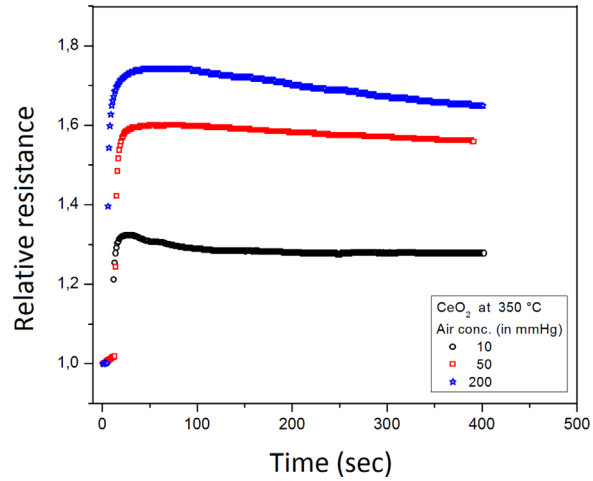

Fig. 5. Electrical resistance versus time as a function of air content of films synthesized from the nanoparticles obtained at 100 °C in the MAH.

1 (R_{co}/R_v). This is a consequence of the CO adsorption onto to the surface that, despite the long time of CO exposure, indicates that there is not reaction due to the the small oxygen amount on to the surface.

Both oxygen and CO adsorption processes onto the grains, when films are previously treated in vaccum at 500 °C, provokes an increasing in the barrier height due to the formation of acceptor centers on to the surface, and a decrease of the conductivity appears [25]. In particular oxygen adsorption generates deeper acceptors levels than CO and consequently higher potential barriers are formed.

Fig. 5 evidences the relative electrical response (R_{air}/R_v vs. time) of the sample F_8 after changing the vacuum into oxygen, in a static-atmosphere chamber with oxygen pressures of 0, 10, 50 and 200 mmHg. The experiments were carried out at 350 °C. Fig. 5 shows that after a quick increasing due to oxygen exposure during a lapse of approximately 25 s, a diminution in the resistance is observed. Resistance versus time curves can be understood by considering that intergranular potential barriers are responsible for the observed electrical response. The rapid increase of the resistance, when samples are exposed to oxygen, indicates that equilibrium at the surface is quickly reached. The interaction of oxygen with grain surfaces produces the transfer of electrons from the bulk to the surface. From this process, the barrier height and the depletion width become larger and, as a consequence, the sample resistance increases. The subsequent slow change in the electrical response needs a more subtle discussion. In a previous work, we proposed that oxygen diffusion into the grains is responsible for these slow changes in resistance by affecting the oxygen vacancies concentration and the Schottky barrier widths.

Furthermore, we proposed a cluster model to explain gas sensor of complex metal device of CeO_2. In this cluster model, the magnitude and structural order-disorder effects determine their physical properties. CeO_2 has fluorite-like cubic structure, as confirmed by XRD measurements, with each Ce^{4+} ions surrounded by eight O^{2-} ions in face-centered cubic (FCC) arrangement, whereas each O^{2-} ion is tetrahedrally surrounded by four Ce^{4+} ions. The cluster-to-cluster charge-transfer process provides direct insight into charge carrier dynamics in materials, and hole polar on trap states localized at oxygen anions in both, bulk and surface. Oxygen vacancies in a disordered structure with $[CeO_8]^x/[CeO_7 \cdot Vo^x]$ complex clusters are hole trapping centers, according to the following equations:

$$[CeO_8]^x + [CeO_7 \cdot V_o^x] \rightarrow [CeO_8]' + [CeO_7.Vo^{\bullet}] \quad (1)$$

$$[CeO_7 \cdot V_o^x] + O_2 \rightarrow [CeO_7 \cdot V_o^x] \ldots O_2(ads) \quad (2)$$

$$[CeO_7 \cdot V_o^x] \ldots O_2 \rightarrow [CeO_7.Vo^{\bullet}] \ldots O_2'(ads) \quad (3)$$

$$[CeO_7{\cdot}V_o^x]+[CeO_7{\cdot}V_o']\ldots O_2' \rightarrow 2[CeO_7.Vo^{\bullet}]\ldots O' \quad (4)$$

$$[CeO_7{\cdot}Vo^{\bullet}]\ldots O' \rightarrow [CeO_7{\cdot}Vo^{\bullet\bullet}]\ldots O'' \quad (5)$$

It is generally accepted that oxygen vacancies in semiconductor oxides act as electron donors and thus they tend to increase the conductivity of the film. It is known that, after oxygen diffusion into the grain, the oxygen vacancy concentration is reduced, the depletion width of intergrain barriers becomes larger and the barriers heights are not altered. This corresponds to the observed behavior in F_8 after oxygen exposure at working temperature. Thus, due to a lower electron density and wider barriers, that reduces thermionic and tunneling currents, the sample conductivity decreases. At 350 °C the oxygen diffusion into the grains is significant and the bottom of the overlapped potential barriers increases. Particularly, in Fig. 5, the electrical resistance decrease (after oxygen exposure) at low response time (30 s) can be observed. This phenomena indicates that vacancies are annihilated as a consequence of the oxygen diffusion process into the grains.

The action of CO gas on the CeO_2 surface can be addressed by Eqs. (1)–(8) which shows that the sensor response is quite fast, but the saturation time is different for adsorption and desorption processes.

$$[CeO_7{\cdot}Vo^{\bullet}]\ldots O_2' + CO \rightarrow [CeO_7{\cdot}V_o^x]\ldots CO\,(ads)+O_2 \quad (6)$$

$$2\,[CeO_7\cdot Vo^{\bullet}]\ldots O'+2CO\rightarrow 2[CeO_7\cdot Vo^x]\ldots CO\,(ads)+O_2 \quad (7)$$

$$2\,[CeO_7\cdot Vo^{\bullet\bullet}]\ldots O''+2CO\rightarrow [CeO_7\cdot Vo^x]\ldots CO\,(ads)+O_2 \quad (8)$$

In Fig. 6 we present resistance vs. time curves for different CO pressures. At this point, it is necessary to remark that the sample was previously treated in an oxygen atmosphere and had a high amount of oxygen adsorbed onto the surface and into the grains. Then, when samples are exposed to CO, the following processes can be taken into account:

1) *CO adsorption*. Carbon monoxide adsorption on a clean surface produces an increasing of the barrier height and a diminution in the sample conductivity as shalows acceptors levels are generated. (See Fig. 4, when the F_8 film is exposed to CO-when samples are previously treated in vaccum- for all temperature range)
2) *Reactions with CO*. At temperatures greater than 180 °C, carbon monoxide reacts with adsorbed oxygen on the CeO_2 surface according to following equations [26]

$$2\,CO+O_2^- \rightarrow 2\,CO_2+e^- \qquad (T < 100\,°C), \quad (9)$$

$$CO+O^- \rightarrow CO_2+e^- \qquad (100\,°C < T < 300\,°C), \quad (10)$$

$$CO+O_2^- \rightarrow CO_2+2e^- \qquad (T > 300\,°C), \quad (11)$$

This reduction in the oxygen amount makes the sample conductivity higher.
3) *Diffusion out of the grains*. It is generally accepted that oxygen vacancies in semiconductor oxides act as electron donors and thus they tend to increase the conductivity of the film. After the whole previous oxygen, adsorbed onto the surface, react with CO, oxygen diffusion out of the grain occurs to continue reaction with CO. Then the oxygen vacancy concentration is increased; the depletion width of intergrain barriers becomes narrower while the barriers heights are not altered. Thus, due to a higher electron density and thinner barriers that increases, specially, tunneling currents, the sample conductivity increases.

Considering processes 1–3, it can be deduced from Fig. 6, that for CeO_2 film, when the atmosphere is changed from vacuum to CO, the reaction is favoured as temperature and CO concentration increase. As temperature increases, from 200 °C, the conversion rate of CO to CO_2 raises when CO concentration changed from 10 to 50 mmHg. A conversion rate saturation was found for CO concentrations greater than 50 mmHg.

Fig. 7 shows the Raman spectrum of F_8 film after CO treatment. The spectrum is dominated by the strong F_{2g} mode of CeO_2 fluorite phase at 462 cm^{-1} with others bands at 586, 710, 858 and 1175 cm^{-1}. The 586 cm^{-1} band corresponds to a shift of the 603 cm^{-1} Raman band seen on the initial powder (Fig. 2) to lower Raman wavenumbers, with a shoulder band at 555 cm^{-1}. The relative intensity ratio of I_{586}/I_{462} for F_8 film after CO treatment increases considerably with regard to the sample before treatment, indicating that the CO reduction introduce more intrinsic defect sites on ceria. Furthermore, Wu et al. [23] indicate that the shoulder at 560 cm^{-1} is due to the presence of oxygen vacancies created during reduction of ceria. Therefore, the shoulder band at 555 cm^{-1} in Fig. 7 is a directly proof to O-vacancies on reduced samples after CO treatment.

Now, we will estimate the barrier height and donor concentration for films thermally treated in vacuum atmosphere (10^{-4} mmHg), as can be seen in Fig. 8. In order to gain confidence in our studies and obtain activation energies, conductance vs. 1/Temperature measurements were carried out. In particular, an

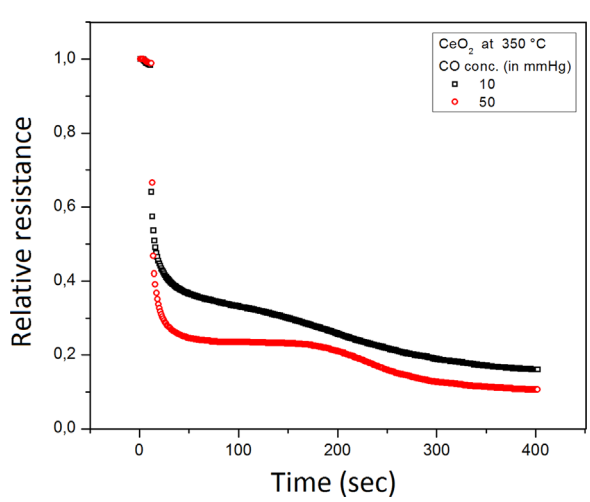

Fig. 6. Electrical resistance versus time as a function of CO content of film conformed with the synthesized nanoparticles obtained at 100 °C in the MAH (F_8). (a) 10 mmHg and (b) 50 mmHg.

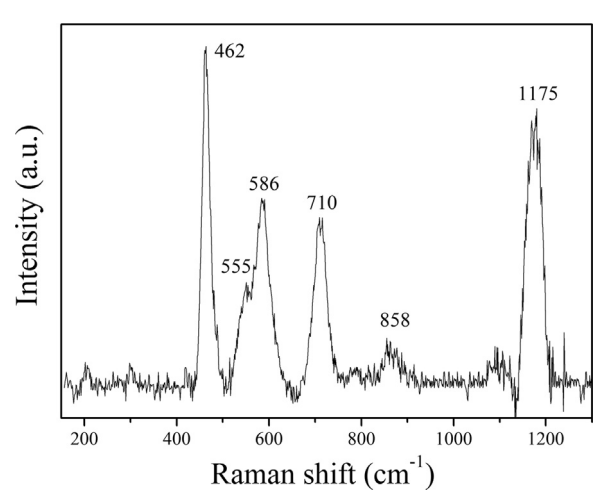

Fig. 7. Raman spectrum of F_8 film after CO treatment.

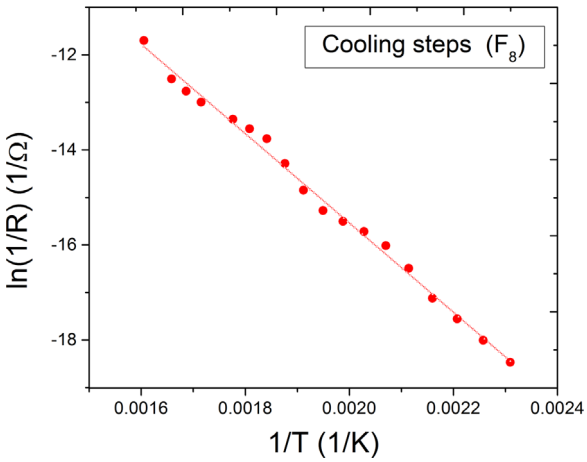

Fig. 8. Arrhenius plot for the F_8 film.

"*Arrhenius plot*" for the CeO_2 film under vacuum is shown. The data were obtained after a first cooling down from 350 °C to 25 °C, when the conductivity as a function of temperature was single-valued. It is important to note that many authors consider that the Schottky barrier height (Φ) can be assumed to be the activation energy (Ea). At this point, it is important to note that assuming $\Phi = Ea$ implies that the three following conditions must be considered:

a) No gas adsorption/desorption takes place during the heating or cooling processes.
b) Non overlapped potential barriers.
c) No oxygen diffusion into or out of the grains occurs during the heating or cooling within the temperature range of the study.

Then, according to our studies, to consider $\Phi = Ea$, only vacuum cycles could be used. As a first approximation, assuming an Arrhenius relation and thermionic-field assistant currents, the total current density over and through a barrier can be calculated in vacuum as [27,28]:

$$J = \frac{AT}{k}\int_0^{V_s} f(E)P(E)dE + AT^2\exp(-e\phi/kT) \tag{12}$$

The first term corresponds to the tunneling current and the second to the thermionic current, A and k are the Richardson and Boltzmann constants, and $f(E)$ is the Fermi-Dirac distribution. $P(E)$, the transmission probability for a reverse-biased Schottky barrier (which is the limiting step, as was explained by Castro et al. and C. R. Crowell et al. [29]) is given by

$$P(E) = \left\{\exp - \left[\frac{4\pi V_s}{qh}\left(\frac{m\varepsilon}{N_d}\right)^{1/2} \ln\left(1 - \frac{(1-\beta)^{1/2}}{\beta^{1/2}}\right)\right]\right\} \tag{13}$$

where m is the electron effective mass, ε the electrical permittivity ($\varepsilon_r = 20$ for CeO_2), h the Planck constant and β is E/ϕ. The experimental current density (J_{exp}) can be obtained from the grain boundary resistance (Fig. 8) with the following relationship:

$$J = V/SR_{gb(f\to 0)} \tag{14}$$

where V is the applied voltage during impedance spectroscopy measurements, S the block electrode area (6.5×10^{-5} m^2) and R_{gb} the grain boundary resistance measured at low frequencies (DC multimeter measurement). Then, a pair of N_d and Φ values were used for fitting the experimental values with Eqs. (12)–(14). Iterative calculations were carried out until the calculated total current (thermionic and tunnel current) was equal to the experimental value obtained with Eq. (12). The resulting N_d and Φ values, can be interpreted as the donor concentration and the barrier height when samples meet those three conditions (a–c). Considering that the sample was exposed at 350 °C, under vacuum, and due to oxygen desorption and also considering that oxygen diffuses out of the grains, an increasing of the vacancies density is expected. The pairs of N_d and Φ values for F_8 films obtained from iterative calculations, adjusting the experimental data was determined being $\Phi = 0.88$ (eV) and Nd $= 1.5 \times 10^{24}$ (1/m^3) (Table 1). For air and CO exposure, barrier height and donor concentration cannot be estimated. This is not only on account the conductance mechanism of a semiconductor thermally favoured (thermionic and tunnel conductions function of temperature) is involved, but gas diffusion, gas adsorptions and reactions, in the case of CO, are present. As a consequence of these phenomena the interfaces between grains are not in a dynamical equilibrium, and barrier height determination in these situations can lead to mistaken results [30].

Table 1
N_d and ϕ values for F_8 films conformed with the synthesized powders from the nanoparticles obtained at 100 °C in the MAH.

	Φ (eV)	Nd × 10^{24} (1/m^3)
Vacuum	0.88	1.5

The dashed line illustrated in Fig. 8 corresponds to a linear fitting (using Eqs. (12)–(14)) of the experimental results of the measured conductivity. Despite that vacuum atmosphere favours the electrical conduction of the film (F_8 the tunneling current is dominant along the whole temperature range).

A bar diagram of current densities rates as a function of temperature for sample films is shown in Fig. 9. The electrical conduction of undoped CeO_2 films thermally treated in vacuum atmosphere is dominated by tunneling current. This conclusion is a good indication that the sensor response of CeO_2 film originates from intrinsic defects and charge transfer after a certain degree of structural order. Probably, the sensor response is arising from the contribution of different intermediary energy levels within the band gap. This behavior is not associated to the band-to-band emission process due to the wavelength's energy (2.54 eV) to be smaller than the E_g of CeO_2 film. Also, this behavior can be associated with the formation of superficial defects caused by the modifications on the morphology of these films [31]. These defects are arising from rapid heating, high effective collision rates between the small particles and growth processes during the processing of CeO_2 nanoparticles. As temperature increases an

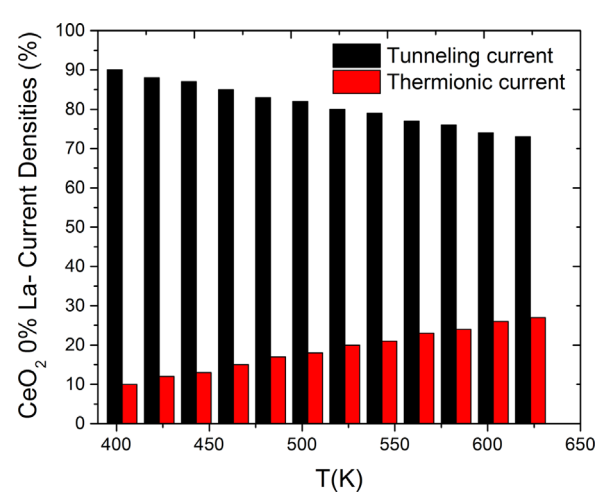

Fig. 9. A bar diagram of current densities rates as a function of temperature for F_8.

increase of thermionic current is observed.

4. Conclusions

XRD results confirmed that CeO_2 powders with different times of synthesis exhibit similar behavior and can be well-indexed in a pure cubic structure of (space group: *Fm*3*m*) with lattice constant a = 5.411 Å. Using Raman Spectroscopy we have shown that carbon monoxide treatment of CeO_2 films conduce to an increase of intrinsic defects. This phenomena was a directly proof of an increase of the oxygen vacancies on reduced samples after CO treatment. The electrical conduction of undoped CeO_2 films thermally treated in vacuum atmosphere is dominated by the tunneling current. This conclusion is a good indication that the sensor response of CeO_2 film originates from intrinsic defects and charge transfer after a certain degree of structural order. Probably, the sensor response is arising from the contribution of different intermediary energy levels within the band gap. This behavior is not associated to the band-to-band emission process due to the wavelength's energy (2.54 eV) to be smaller than the E_g of CeO_2 film.

Acknowledgments

The financial support of this research project by the Brazilian research funding agencies CNPq (National Council for Scientific and Technological Development) 573636/2008-7, INCTMN 2008/57872-1 and FAPESP (São Paulo Research Foundation) 2013/07296-2.

References

[1] C.B. Murray, D.J. Norris, M.G. Bawendi, Synthesis and characterization of nearly monodisperse CdE (E = sulfur, selenium, tellurium) semiconductor nanocrystallites, J. Am. Chem. Soc. 115 (1993) 8706–8715.
[2] X. Wang, J. Zhuang, Q. Peng, Y. Li, A general strategy for nanocrystal synthesis, Nature 437 (2005) 121–124.
[3] J. Hu, L.-S. Li, W. Yang, L. Manna, L.-W. Wang, A.P. Alivisatos, Linearly polarized emission from colloidal semiconductor quantum rods, Science 292 (2001) 2060–2063.
[4] A.P. Alivisatos, Semiconductor clusters, nanocrystals, and quantum dots, Science 271 (1996) 933–937.
[5] P. Jasinski, T. Suzuki, H.U. Anderson, Nanocrystalline undoped ceria oxygen sensor, Sens. Actuators, B 95 (2003) 73–77.
[6] S. Park, J.M. Vohs, R.J. Gorte, Direct oxidation of hydrocarbons in a solid-oxide fuel cell, Lett. Nat. 404 (2000) 265–270.
[7] T. Meng, M. Ara, L. Wang, R. Naik, K.Y. Simon, Enhanced capacity for lithium–air batteries using $LaFe_{0.5}Mn_{0.5}O_3$–CeO_2 composite catalyst, J. Mater. Sci. 49 (2014) 4058–4066.
[8] K. Sohlberg, S.T. Pantelides, S.F. Pennycook, Interactions of hydrogen with CeO_2, J. Am. Chem. Soc. 123 (2001) 6609–6611.
[9] A. Trovarelli, Catalytic properties of Ceria and CeO_2-containing Materials, Catal. Rev. Sci. Eng. 38 (1996) 439–520.
[10] C.W. Raubach, L. Polastro, M.M. Ferrer, A. Perrin, C. Perrin, A.R. Albuquerque, P. G.C. Buzolin, J.R. Sambrano, Y.B.V. de Santana, J.A. Varela, E. Longo, Influence of solvent on the morphology and photocatalytic properties of ZnS decorated CeO_2 nanoparticles, J. Appl. Phys. 115 (2014) 213514.
[11] B.C. Yadav, Rama Singh, Satyendra Singh, Investigations on humidity sensing of nanostructured tin oxide synthesised via mechanochemical method, J. Exp. Nanosci. (2012) 1–14.
[12] M. Franke, T. Koplin, U. Simon, Metal and metal oxide nanoparticles in chemiresistors: does the nanoscale matter? Small 2 (2006) 36–50.
[13] G. Sakai, N. Matsunaga, K. Shimanoe, N. Yamazoe, Theory of gas-diffusion controlled sensitivity for thin film semiconductor gas sensor, Sens. Actuators B 80 (2001) 125–131.
[14] T. Maekawa, K. Suzuki, T. Takada, T. Kobayashi, M. Egashira, Odor identification using a SnO_2-based sensor array, Sens. Actuators B 80 (2001) 51–58.
[15] M. Kanamori, K. Suzuki, Y. Ohya, Y. Takahashi, Analysis of the change in the carrier concentration of SnO_2 thin film gas sensors, J. Appl. Phys. 33 (1994) 6680–6683.
[16] Y. Shimizu, M. Egashira, Basic aspects and challenges of semiconductor gas sensors, MRS Bull. 24 (1999) 18–24.
[17] G. Gaggiotti, A. Galdikas, S. Kaciulis, G. Mattogno, A. Setkus, Surface chemistry of tin oxide based gas sensors, J. Appl. Phys. 76 (1994) 4467–4471.
[18] R.C. Deus, M. Cilense, C.R. Foschini, M.A. Ramirez, E. Longo, A.Z. Simões, Influence of mineralizer agents on the growth of crystalline CeO_2 nanospheres by the microwave-hydrothermal method, J. Alloy. Compd. 550 (2013) 245–251.
[19] C.S. Ricardi, R.C. Lima, M.L. Dos Santos, P.R. Bueno, J.A. Varela, E. Longo, Preparation of CeO_2 by a simple microwave–hydrothermal method, Solid State Ion. 118 (2009) 288–291.
[20] R.C. Deus, J.A. Cortés, M.A. Ramirez, M.A. Ponce, J. Andres, L.S.R. Rocha, E. Longo, A.Z. Simões, Photoluminescence properties of cerium oxide nanoparticles as a function of lanthanum content, Mater. Res. Bull. 70 (2015) 416–423.
[21] I. Kosacki, T. Suzuki, H.U. Anderson, P. Colomban, Raman scattering and lattice defects in nanocrystalline CeO_2 thin films, Solid State Ion. 149 (2002) 99–105.
[22] S. Wang, W. Wang, J. Zuo, Y. Qian, Study of the Raman spectrum of CeO_2 nanometer thin films, Mater. Chem. Phys. 68 (2001) 246–248.
[23] Z. Wu, M. Li, J. Howe, H.M. Meyer, S.H. Overbury, Probing defect sites on CeO_2 nanocrystals with well-defined surface planes by Raman spectroscopy and O_2 adsorption, Langmuir 26 (2010) 16595–16606.
[24] C. Hess, Investigation of ceria by combined Raman, UV–vis and X-ray photoelectron spectroscopy, Catal. Commun. 22 (2012) 39–42.
[25] N. Barsan, U. Weimar, Conduction model of metal oxide gas sensors, J. Electroceram. 7 (2001) 143–167.
[26] S.M.A. Durrani, M.F. Al-Huhaili, I.A. Bakhtiari, Carbon monoxide gas-sensing properties of electron-beam deposited cerium oxide thin films, Sens. Actuators, B 134 (2008) 934–939.
[27] C.M. Aldao, D.A. Mirabella, M.A. Ponce, A. Giberti, C. Malagù, Role of intragrain oxygen diffusion in polycrystalline tin oxide conductivity, J. Appl. Phys. 109 (2011) 063723.
[28] S.M. Sze, R. Morrison, Chemical Sensing with Solid State Devices, John Wiley & Sons, Inc, New York 1994, pp. 383–414.
[29] C.R. Crowell, V.L. Rideout, Normalized thermionic-field (T-F) emission in metal-semiconductor (schottky) barriers, Solid-State Electron. 12 (1969) 89.
[30] F. Schipani, C.M. Aldao, M.A. Ponce, Schottky barriers measurements through Arrhenius plots in gas sensors based on semiconductor films, AIP Adv. 2 (2012) 032138.
[31] B.P. Falcão, J.P. Leitão, J.C. González, M.R. Correia, C.F. Leite, A.G. de Oliveira, K. G. Zayas-Bazán, F.M. Matinaga, M.B. Moreira, Photoluminescence study of GaAs thin films and nanowires grown on Si(111), J. Mater. Sci. 48 (2013) 1794–1798.